Nonlinear loading of a two-dimensional heaving box

Marcos Rodriguez, Johannes Spinneken*, Chris Swan

Imperial College London, Department of Civil and Environmental Engineering, London SW7 2AZ, UK

Abstract

A numerical investigation is presented addressing the nonlinear heave response of a rectangular box. The work specifically concerns the importance of the relative body dimensions, expressed through the product of the half-beam b and the wavenumber k. When subjected to moderately steep incident waves, the second-harmonic content of the heave motion is found to be as large as 25% of the first-harmonic content. In considering the extent of this second-harmonic motion, three regimes may be defined: (i) the long wave regime, where $kb \leq 0.4$, (ii) an intermediate regime, where $0.4 < kb < 1.0$ and (iii) the diffraction or short wave regime where the $kb \geq 1.0$. Expressed in terms of the wavelength $\lambda = 2\pi/k$, these regimes correspond to (i) $b \leq 0.06\lambda$, (ii) $0.06\lambda < b < 0.16\lambda$ and (iii) $b \geq 0.16\lambda$ respectively. The second-harmonic motion content is found to be particularly pronounced in regimes (i) and (iii). Perhaps surprisingly, this second-harmonic content is also found to be practically non-existent for some intermediate cases lying within regime (ii). Three sources of nonlinearity are shown to be particularly important. First, the interaction between the first-order incident waves and the first-order scattered waves is key to the nonlinear loading in regime (iii). Second, the generation of freely propagating second-harmonic radiated waves due to the body motion is important in (i). Third, the local standing wave field associated with the radiation problem is found to contribute to the loading in regime (iii). In addition, the location of the body resonance also plays a critical role in defining the extent of the second-harmonic motion content. The focus of the present work lies on a clear physical interpretation of the sources of these nonlinear loads, coupled with an analysis of the body dynamics.

Keywords: Floating structure, Nonlinear diffraction, Nonlinear radiation, Potential flow, Boundary element method, Rectangular box

*Corresponding author

Email address: j.spinneken@imperial.ac.uk (Johannes Spinneken)

1. Introduction

1.1. The nonlinear radiation-diffraction problem

In many practical applications, the floating body problem is separated into two linearly-independent problems: (A) the excitation problem and (B) the radiation problem. Within the excitation problem, the structure is considered fixed in position and the so-called excitation forces are determined. In contrast, the radiation problem concerns the forced motion of a body and its hydrodynamic properties based on the radiated wave field. Adopting linear superposition, (A) and (B) are combined to model the freely-floating response of a structure.

There are many load cases where a linear hydrodynamic analysis is inadequate. Common examples include a body being driven by steep incident waves or one undergoing large body excursions. Any nonlinear interactions that arise in either the incident wave field or the body's (motion) response prohibit the use of linear superposition. These nonlinear interactions lead to considerably more challenging formulations, which are difficult to solve analytically (or semi-analytically) beyond second order.

Significant effort has been made to develop radiation-diffraction solutions valid to second order. The main difficulty in obtaining such solutions lies in satisfying the inhomogeneous second-order free surface boundary condition. To overcome this difficulty, both Molin (1979) and Lighthill (1979) adopted an indirect approach in which the second-order diffraction forces are evaluated without explicitly calculating the second-order potential. Solutions of this type rely on the evaluation of a free surface integral. In this context, Eatock Taylor and Hung (1987) and Molin and Marion (1985) developed solutions to efficiently calculate this integral by making assumptions about the behaviour of the second-order potential at large distances from the body.

Kim and Yue (1989, 1990) extended this earlier work, achieving a full and direct solution of the velocity potential for both monochromatic and bichromatic waves. A 'partially nonlinear' approach, which addresses linear (small amplitude) incident waves but considers diffraction effects up to second order, was presented by Sulisz (1993). Within this solution a method of matched eigenfunction expansions is used to solve the Boundary Value Problem (BVP) for a fixed rectangular body. This produces a complete expression for the velocity potential in two dimensions.

All of the solutions noted above were formulated in the frequency domain. Alongside this work advances in computational resources have enabled the development of fully-nonlinear time-domain solvers, commonly relying on a Boundary Element Method (BEM). Nonlinear BEM formulations have been shown to efficiently model a wide variety of scenarios related to wave generation and evolution, as demonstrated by Longuet-Higgins and Cokelet (1976), Grilli and Horrillo (1997), Hague and Swan (2009), Christou et al. (2009) and Spinneken et al.

(2014). In addition to capturing the full extent of the nonlinear interactions, fully-nonlinear descriptions also offer benefits in terms of implementation and convergence. These type of approaches avoid the need for any special treatment of the slowly converging free surface integrals commonly reported in second-order formulations. Indeed, despite appearing to be more challenging due to their nonlinear formulation, the implementation and convergence of fully-nonlinear time-domain solutions can often be less challenging than that of second-order formulations. The only drawback of applying a fully-nonlinear solution lies in the computational effort associated with the time marching. However, in a two-dimensional context, the relatively low number of computational nodes ensures that this is not a barrier to its effective implementation.

Other examples of nonlinear diffraction methods include the work by Ma et al. (2001), in which a finite element method was used to compute the three-dimensional interaction between steep incident waves and fixed bodies. Results were presented for the nonlinear diffraction around a vertical cylinder incorporating both monochromatic and bichromatic incident waves. Xue et al. (2001) used a mixed Eulerian-Lagrangian high-order boundary element method to investigate nonlinear diffraction scenarios in three dimensions. This includes the generation of bow waves from ships and the 'ringing' loads on a surface-piercing vertical cylinder in steep regular waves. Ferrant et al. (2003) provided a related investigation, again undertaken in the time domain, in which a BEM implementation of the initial boundary-value problem was used to investigate the nonlinear diffraction by arbitrary 3D structures. In the context of the nonlinear radiation problem, notable contributions include Maiti and Sen (2001), Bai and Eatock Taylor (2006) and Zhou et al. (2013).

1.2. Nonlinearities in the floating body problem

Building upon the available body of work, the present study seeks to advance the understanding of the coupled floating-body problem. Specifically, the work aims to:

(i) provide guidance as to the applicability of commonly adopted linear descriptions

(ii) quantify the extent of the nonlinearities arising

(iii) explain, in physical terms, the origin of the nonlinear forcing components

To address these points, a nonlinear potential flow solver was applied to the description of a heaving rectangular box. The calculations were undertaken in the time domain; the box placed within a Numerical Wave Tank (NWT) based on a boundary element scheme. Full details of the NWT formulation are provided in §2. At this stage it is instructive to demonstrate the problem by way of an example.

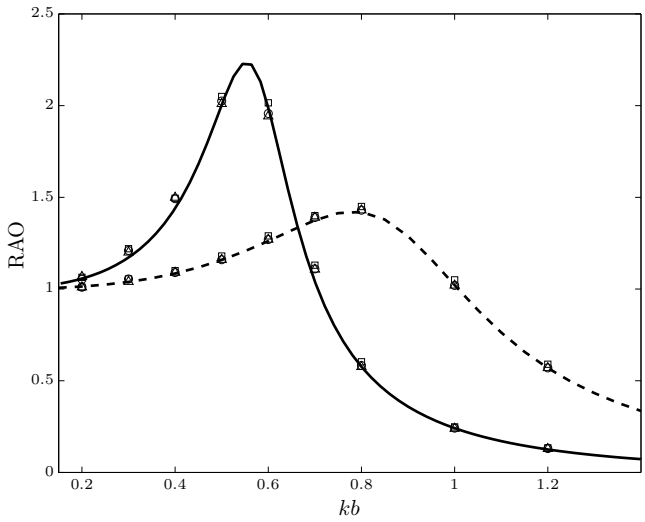


Figure 1: Heave Response Amplitude Operator (RAO) for a rectangular box subjected to regular waves with A_ik = (a) $\triangle$ 0.01, (b) $\circ$ 0.05, (c) $\square$ 0.10 (present nonlinear computations for RB2) and ▬ ▬ Linear RAO RB1, ▬▬ Linear RAO RB2, where the geometries of cases RB1 and RB2 are as outlined in Table 1(a).

In order to analyse the behaviour of a floating structure, the Response Amplitude Operator (RAO) is commonly obtained. This defines the ratio between the linear motion response and the linear incident wave amplitude. In the present nonlinear computations, the RAO was obtained by evaluating the magnitude of the first-harmonic heave displacement time history, allowing sufficient initial simulation time to reach a steady state.

Figure 1 illustrates the magnitude of the heave RAO for a box of draught $d = 0.2h$, where h is the water depth, and half-beam $b = d$; this box geometry being referred to as RB2 hereafter. The figure also contains data relating to an alternative configuration RB1 (dashed line) which will be discussed later on. Considering box RB2, the figure shows both the linear RAO (solid line) obtained using a commercial radiation-diffraction solver (WAMIT, 2013) and the RAO from the present nonlinear computations (discrete symbols). For the purpose of the nonlinear computations, the heave displacement ξ was excited by moderately steep regular waves of wavenumber k and amplitude A_i, where the subscript i denotes the incident wave condition. The wavenumber k is the solution to the well known linear dispersion equation $\omega^2 = gk \tanh kh$, where ω is the circular wave frequency and g denotes acceleration due to gravity. The nonlinearity or steepness of the incident wave field is defined by A_ik. Within Figure 1 three distinct cases are considered: (a) $A_ik = 0.01$ (symbol $\triangle$), (b) $A_ik = 0.05$ (symbol $\circ$) and (c) $A_ik = 0.10$ (symbol $\square$).

Figure 1 shows close agreement between the (linear) industry-standard approach and the present nonlinear computations; the maximum departure being 5% for all cases considered. Clearly, the effect of the wave steepness on the RAO is very limited. This observation is also confirmed for box RB2 (dashed line). The close agreement in the RAO is perhaps surprising,

given that the steepness of the incident regular waves is up to $A_i k = 0.1$. However, Figure 1 only considers the amplitude of the first-harmonic motion, which is not affected by second-order quantities. Indeed, the first harmonic is only affected by interactions arising at the third, fifth and higher uneven orders. As a result, if the nonlinearities of the motion are primarily driven by effects arising at second order, comparisons based on the RAO are not informative. To demonstrate this further, Figure 2 shows the normalised time histories of the heave motion, ξ/d, for three select wave cases characterised by:

(1) Case 1, Figure 2(a): $A_i k = 0.1$ and $kb = 0.2$ ($b \approx 0.03\lambda$)

(2) Case 2, Figure 2(b): $A_i k = 0.1$ and $kb = 0.6$ ($b \approx 0.1\lambda$)

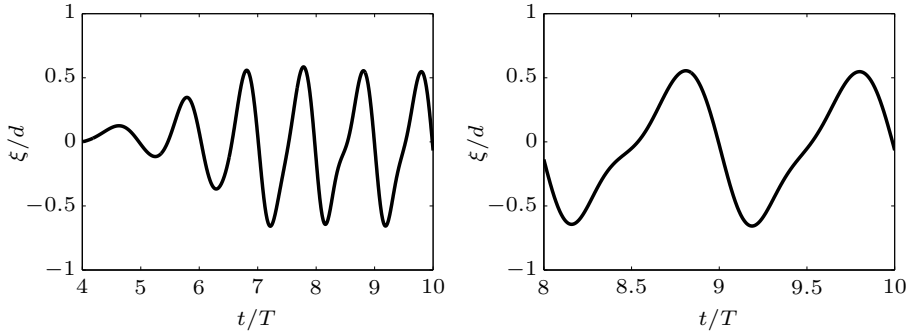
(3) Case 3, Figure 2(c): $A_i k = 0.1$ and $kb = 1.2$, ($b \approx 0.2\lambda$)

In all three cases, the body geometry ($d = 0.2h$ and $b = d$) was held constant. Each case is presented in two parts; the left hand side showing the time history of the heave motion including the initial transient response, and the right hand side a close-up of two wave periods in which the steady-state response is established. In each case, the transient response is due to at least three effects. These include wave propagation into initially still water, a ramp-up function applied at the input boundary, and the body accelerating from its rest position. In all figures the horizontal axis shows the simulation time t normalised by the wave period $T = 2\pi/\omega$.

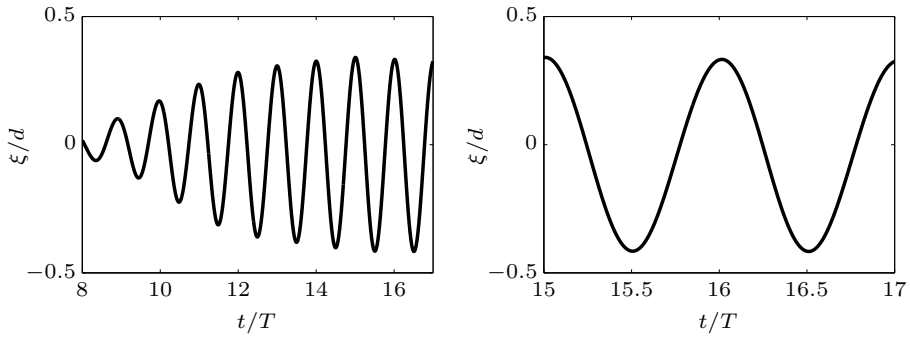
Observing Figure 2, it is clear that both Cases 1 and 3 are associated with significant motion nonlinearities. In Case 1 a significant higher harmonic component is clearly present, while in Case 3 the motion is highly asymmetric about the equilibrium position. In contrast, the heave motion in Case 2 is closely approximated by a single sinusoid. Further analysis of the data presented on Figure 2 showed that the nonlinearities occurred primarily at the second-harmonic of the incident wave frequency. Interestingly, the nonlinearities were found to be pronounced at low kb ($kb \approx 0.2$) and high kb ($kb \approx 1.2$), but were practically non-existent for some intermediate values. Evidence of this is provided by the fact that in Case 1 (Figure 2(a), $kb = 0.2$) the amplitude of the second harmonic is approaching 25% of the first harmonic, while in Case 2 (Figure 2(b), $kb = 0.6$) the second-harmonic motion content was less than 1% of the first-harmonic motion.

1.3. Scope of the present work

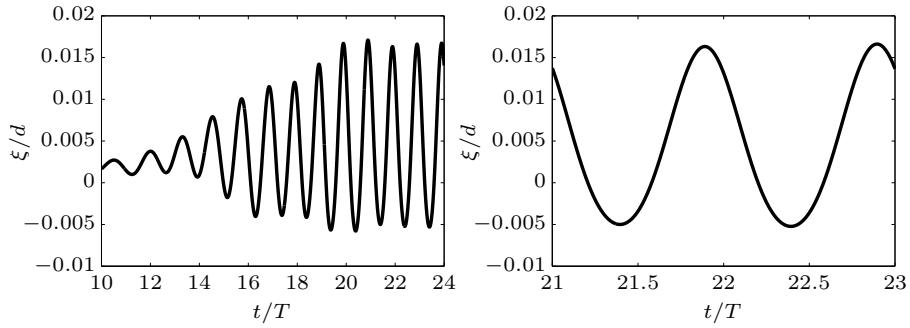
In the context of the above discussion, the purpose of the present paper is to provide a physical explanation for the nonlinearities associated with the floating body problem. Specifically, the work seeks to quantify the influence of the relative body dimension kb on the extent of the nonlinear forcing and the nonlinear motion. To limit the scope of the



(a) Case 1: $kb = 0.2$



(b) Case 2: $kb = 0.6$



(c) Case 3: $kb = 1.2$

Figure 2: Time history of the normalised heave motion ξ/d for a rectangular box with $d = 0.2h$ and $b = d$ subjected to regular waves of steepness $A_i k = 0.1$.

paper, some simplifications must be made. First, the geometry is restricted to a heaving, semi-submerged rectangular box in two dimensions. Second, the analysis will focus on second-order effects; higher-order effects being the subject of a future investigation. Third, the problem is limited to regular waves and the corresponding steady-state response.

The paper continues with the numerical formulation outlined in §2. To isolate the non-linearities in each part of the solution, the numerical computations are then considered in three distinct parts: (A) the excitation problem, (B) the radiation problem, and (C) the coupled floating body problem. These are addressed in §3, §4 and §5 respectively. The paper concludes in §6, summarising the key findings of the present work, and commenting on their importance for alternative (non-rectangular) geometries.

2. Problem definition

2.1. Numerical model

The numerical method adopted in the present work is based upon the Multiple-flux BEM (MFBEM) approach introduced by Hague and Swan (2009). This method is implemented as a NWT; the model being analogous to an actual physical wave tank. Within this numerical domain of length L and water depth h, a semi-submerged rectangular body of draught d, half-beam b and mass m intersects the free surface (Figure 3). The numerical domain is bound by a horizontal and impermeable bed, Γ_{-h}, a wave input boundary, Γ_i, the free surface, Γ_s, the body surface, Γ_b, and a wave radiation boundary, Γ_r (Figure 3).

The Cartesian coordinate system (x, z) is located such that $x = 0$ defines the centre of the body and $z = 0$ the Still Water Level (SWL). To simplify the analysis, the motion of the body is restricted to heave. As a result, the motion of all body nodes can be captured in a semi-Lagrangian frame of reference, where nodes only translate in the vertical z direction. Furthermore, $\xi(t)$, $\dot{\xi}(t)$ and $\ddot{\xi}(t)$ denote the time-varying heave displacement, velocity and acceleration respectively. This motion is defined so that a positive heave displacement $\xi(t)$ is aligned with the positive direction of the z axis.

The fluid is assumed to be inviscid and the flow irrotational, allowing the introduction of a velocity potential ϕ. Adopting this, the horizontal and vertical fluid velocities are defined as $(u, w) = (\partial\phi/\partial x, \partial\phi/\partial z)$, and mass continuity, which must hold throughout the fluid domain, is expressed by Laplace's equation,

$$\frac{\partial^2\phi}{\partial x^2} + \frac{\partial^2\phi}{\partial z^2} = 0. \tag{1}$$

In addition to the velocity BVP (expressed in terms of ϕ), the computation of the forces experienced by a moving body may be achieved through the definition of a second BVP.

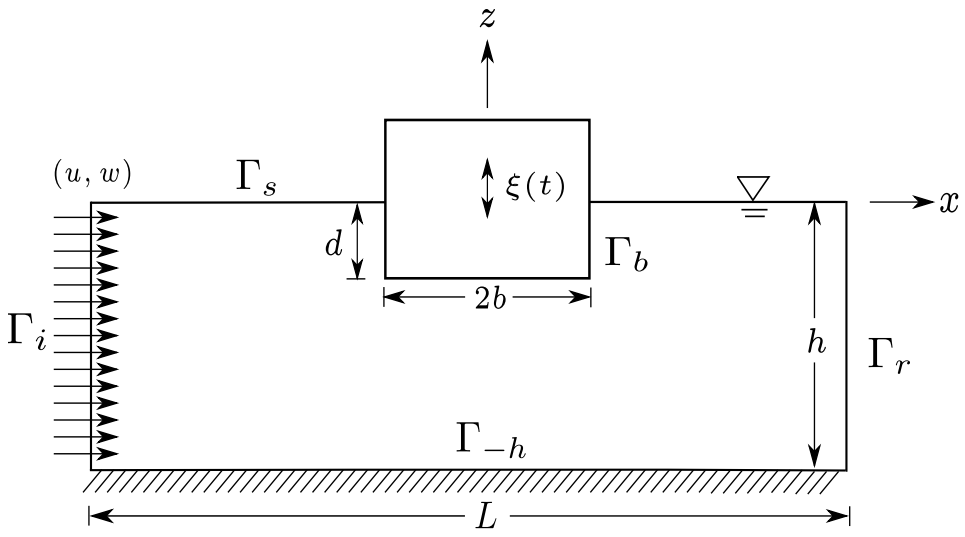


Figure 3: A schematic of the numerical domain (not to scale).

This second approach is commonly referred to as the acceleration BVP, and often defined in terms of an artificial function ψ which also satisfies Laplace's equation (Kashiwagi, 2000). The main aim of the acceleration potential is to eliminate the need to solve for the temporal derivative of the velocity potential, $\partial\phi/\partial t$, in the expression for the wave-induced forces.

The present numerical method combines the MFBEM formulation by Hague and Swan (2009) with the force computation method outlined in Kashiwagi (2000). In practice, the solution is achieved as follows:

(i) The velocity field (u, w) is specified on the input boundary, Γ_i, a radiation condition is imposed on the downstream boundary, Γ_r, and a no-flow condition is adopted on the bed; the latter specified so that $\partial\phi/\partial z = 0$ along the horizontal bed Γ_{-h}. The two fully-nonlinear free surface boundary conditions are applied on the instantaneous free surface Γ_s, where η defines the elevation of the water surface relative to the SWL. These incorporate a kinematic free surface boundary condition (KFSBC)

$$\frac{\partial\eta}{\partial t} = w - u\frac{\partial\eta}{\partial x} \tag{2}$$

and a dynamic free surface boundary condition (DFSBC)

$$\frac{d\phi}{dt} = -g\eta - \frac{1}{2}(u^2 + w^2) + w\frac{d\eta}{dt}. \tag{3}$$

(ii) For the purpose of the excitation problem, waves generated on input boundary, Γ_i, are incident upon a *fixed* rectangular box so that $\xi(t) = 0$. The regular wave kinematics (u, w) input on Γ_i are calculated using the fifth-order solution by Fenton (1985). The

no-flow condition on the fixed body is achieved through $\partial\phi/\partial n = 0$ on Γ_b, where $\partial/\partial n$ denotes the derivative with respect to the outward pointing surface normal, n. The overall solution of the fixed problem is very similar to the scheme described by Christou et al. (2008) and Christou et al. (2009), where the MFBEM was applied in the context of wave diffraction over a submerged breakwater and wave interaction with a vertical wall.

(iii) In considering the radiation problem, the body is subjected to an imposed time-varying velocity $\dot{\xi}(t)$ given by

$$\dot{\xi}(t) = \mathbb{R}\left\{-i\omega\xi_a \exp(-i\omega t)\right\}, \tag{4}$$

where ξ_a is the amplitude of the sinusodial displacement, ω refers to the frequency of the imposed oscillation and $\mathbb{R}$ denotes the real part. The body boundary condition in this particular problem differs from that in which the body is held fixed. Along the body boundary Γ_b, the boundary condition in terms of ϕ is given as

$$\frac{\partial\phi}{\partial n} = \dot{\xi}(t)\cos\theta, \tag{5}$$

where θ corresponds to the angle between the horizontal and the outside surface of the body measured anticlockwise. In contrast to the fixed body case, (ii) above, the vertical position of the body nodes must now be updated using the instantaneous body velocity at each time step. This is straightforward; with the body velocity, $\dot{\xi}(t)$, imposed it does not depend upon the fluid force, F, and is, as such, known *a priori*.

(iv) To resolve the floating body problem, the 'indirect acceleration potential' method (Tanizawa, 1995; Wu and Eatock Taylor, 1996; Kashiwagi, 2000) has been adopted herein. For the heave degree of freedom, the dimensional force F is given by

$$F(t) = -\rho\left(-\ddot{\xi}(t)A_m + Q\right), \tag{6}$$

where A_m serves a similar purpose to the added mass but, in this case, is calculated from the integral of the auxiliary function identified in Kashiwagi (2000). In contrast, Q describes all other force components not dependent upon the acceleration, $\ddot{\xi}(t)$. For full detail of this approach, including a formulation for A_m, Q and the boundary conditions for the artificial function ψ, the reader is referred to Kashiwagi (2000). Adopting Newton's second law, with $F(t) = m\ddot{\xi}(t)$, the unknown body acceleration may be obtained as

$$\ddot{\xi}(t) = \frac{-\rho Q}{m - \rho A_m}. \tag{7}$$

This acceleration may now be integrated numerically to obtain the heave velocity $\dot{\xi}(t)$, feeding directly into the velocity BVP.

In each of the above cases (fixed, radiating, floating) the resulting Boundary Integral Equation (BIE) is discretised and rearranged such that the unknown quantity at each of the domain's nodes (either the potential ϕ or the potential flux $\partial\phi/\partial n$) can be obtained by solving the BIE at each time step. The acceleration BVP, expressed in terms of $\partial\phi/\partial t$ and $\partial^2\phi/\partial t\partial n$, is formulated in an analogous way. The solution is then time-marched, with all integrations (free surface boundary conditions and body velocity) resolved using a fourth-order Runge-Kutta scheme. A set of initial conditions place both the body and the fluid at rest at $t = 0$.

2.2. Test parameters

From the initial discussion of Figure 2, it is clear that the body dimension kb plays an important role in the development of any nonlinearities. To investigate this further, a number of rectangular box configurations are considered. For the majority of the analysis, two base configurations, RB1 and RB2, are investigated. RB1 is characterised by a draught-to-depth ratio of $d/h = 0.1$, with a beam-to-draught ratio of $b/d = 2.0$. In RB2, the draught is extended so that $d/h = 0.2$ and $b/d = 1.0$. In both cases, wave conditions corresponding to the range $0.2 \leq kb \leq 1.2$ will be considered.

3. Part A: Investigation of the nonlinear excitation problem

3.1. Introduction and test parameters

The main test cases considered in the context of the excitation problem are detailed in Table 1(a). This describes the body dimension kb, the non-dimensional water depth kh and the incident wave steepness A_ik. Additional cases with varying wave steepness, A_ik, were also considered as outlined in Table 1(b). Within these tables the entries denoted with the symbol (-) could not be achieved numerically. The reason for this lies simply in the fact that waves cases with large wavelength λ (small k) lead to wave amplitudes A_i in excess of the body draught d, even for relatively limited values of A_ik. Setting aside this issue, the cases described in Table 1 provide a broad range of conditions appropriate to an investigation of the nonlinear excitation problem.

Figure 4 shows sample time histories of the vertical excitation force on box RB2; the incident regular wave train of wave steepness $A_ik = 0.10$ being characterised by (a) $kb = 0.3$, (b) $kb = 0.6$ and (c) $kb = 1.2$. These fixed-box cases are very similar to those considered for the heaving box in Figure 2; the only exception being $kb = 0.3$ since $kb = 0.2$ could not be achieved for $A_ik = 0.1$. The waves generated on the input boundary, Γ_i, propagate into

Base cases					
RB1 $d/h = 0.1$ $b/d = 2.0$			RB2 $d/h = 0.2$ $b/d = 1.0$		
kb	kh	A_ik	kb	kh	A_ik
0.2	1.0	0.05	0.2	1.0	0.05
0.3	1.5	0.05	0.3	1.5	0.05
0.4	2.0	0.05	0.4	2.0	0.05
0.5	2.5	0.05	0.5	2.5	0.05
0.6	3.0	0.05	0.6	3.0	0.05
0.7	3.5	0.05	0.7	3.5	0.05
0.8	4.0	0.05	0.8	4.0	0.05
1.0	5.0	0.05	1.0	5.0	0.05
1.2	6.0	0.05	1.2	6.0	0.05
-	-	-	0.3	1.5	0.10
-	-	-	0.4	2.0	0.10
0.5	2.5	0.10	0.5	2.5	0.10
0.6	3.0	0.10	0.6	3.0	0.10
0.7	3.5	0.10	0.7	3.5	0.10
0.8	4.0	0.10	0.8	4.0	0.10
1.0	5.0	0.10	1.0	5.0	0.10
1.2	6.0	0.10	1.2	6.0	0.10

(a) Base cases

Effect of wave steepness					
RB1 $d/h = 0.1$ $b/d = 2.0$			RB2 $d/h = 0.2$ $b/d = 1.0$		
kb	kh	A_ik	kb	kh	A_ik
0.6	3.0	0.02	0.6	3.0	0.02
0.6	3.0	0.04	0.6	3.0	0.04
0.6	3.0	0.06	0.6	3.0	0.06
0.6	3.0	0.08	0.6	3.0	0.08
0.6	3.0	0.10	0.6	3.0	0.10
0.6	3.0	0.12	0.6	3.0	0.12
-	-	-	0.6	3.0	0.14
-	-	-	0.6	3.0	0.16
-	-	-	0.6	3.0	0.18

(b) Effect of wave steepness

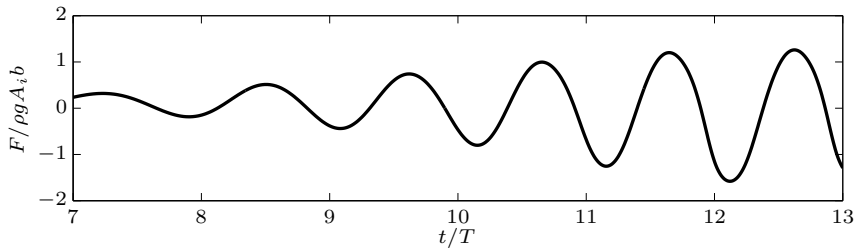
Table 1: Specification of test cases for the wave excitation problem

initially still water. As a result, the body force undergoes a transient response during the initial stages of the simulation. Once a steady-state has been achieved, the nonlinearity of the problem is clearly evident, particularly in Figures 4(b) ($kb = 0.6$) and 4(c) ($kb = 1.2$).

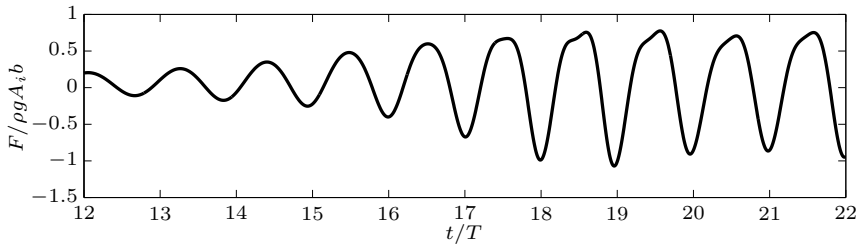
In making a direct comparison to the heaving box problem (Figure 2), different trends may be identified. In the heaving box case, the nonlinear motion was most pronounced for $kb = 0.2$ and $kb = 1.2$, with little nonlinear motion for $kb = 0.6$. In contrast, Figure 4 demonstrates that the nonlinear excitation force increases as kb increases. As in the heaving box problem, these nonlinearities primarily occur at the second harmonic; the drivers for this nonlinear forcing being investigated as follows.

3.2. Second-harmonic excitation forcing

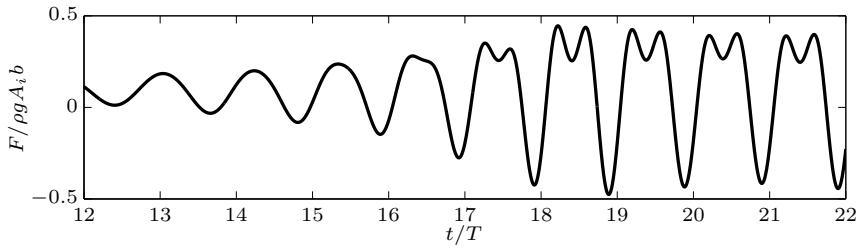
The nonlinear excitation (or diffraction) problem is commonly associated with a nonlinear and freely propagating diffracted wave; the magnitude of this free wave being indicative of the nonlinear forcing. The second-harmonic of this free wave was extracted from the total wave field upstream of the rectangular box by adopting the harmonic decomposition method proposed by Lin and Huang (2004). Given that this methodology assumes all wave components to be progressive, the data used in this analysis was based upon predictions at spatial locations defined by $x \leq -(2h + b)$, or more than $2h$ from the upstream face of the box. This was necessary to avoid the influence of the evanescent wave field that develops adjacent to the box. Considering the progressive wave field only, the harmonic



(a) $kb = 0.3$



(b) $kb = 0.6$



(c) $kb = 1.2$

Figure 4: Time history of the heave excitation force, $F(t)/\rho g A_i b$, for a fixed body with configuration RB2 subjected to regular waves of steepness $A_i k = 0.1$.

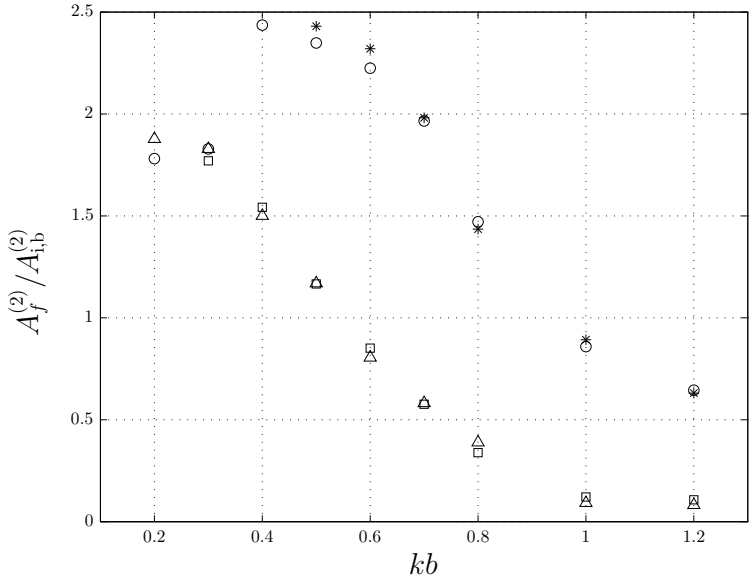


Figure 5: Ratio of diffracted second-harmonic free component to incident second-harmonic bound component for ∘ RB1 with $A_ik = 0.05$, ∗ RB1 with $A_ik = 0.10$, △ RB2 with $A_ik = 0.05$, and □ RB2 with $A_ik = 0.10$; the data having been predicted for $x \leq -(2h + b)$ to avoid contamination from evanescent wave modes.

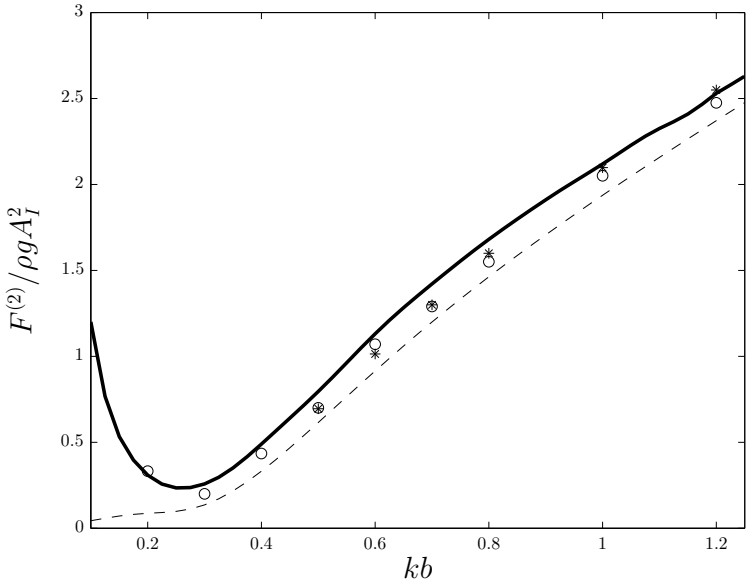
decomposition yields (i) the bound wave (incident and diffracted) content arising at second harmonic and (ii) the free wave content (incident and diffracted) arising at second harmonic.

Figure 5 concerns the ratio of the diffracted free wave, $A_f^{(2)}$, and the incident bound wave, $A_{\mathrm{i,b}}^{(2)}$, indicating that the second-harmonic diffracted free wave is particularly pronounced for small kb. This is in marked contrast to the increased nonlinear forcing with increasing kb observed in Figure 4. It therefore follows that the nonlinear scattered wave field is unlikely to be the primary driver for the pronounced nonlinear excitation forcing shown in Figure 4.

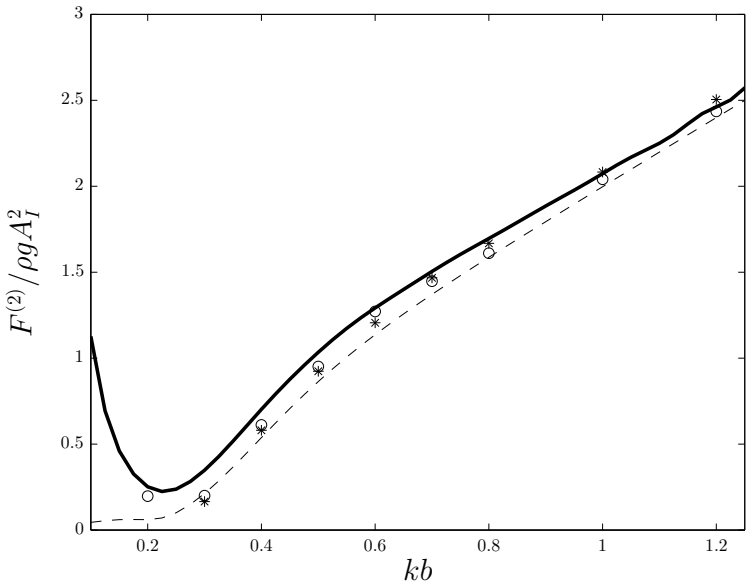
To identify the actual drivers for the nonlinear excitation forcing, the full range of test cases outlined in Table 1(a) was considered. In order to analyse the numerical force time histories, a Discrete Fourier Transform (DFT) was applied to a time window corresponding to an integer number of wave periods taken after the establishment of steady-state conditions. The results of this analysis are illustrated in Figures 6(a) and 6(b), showing the normalised magnitude of the second-harmonic force component $F^{(2)}/\rho g A_i^2$ for configurations RB1 and RB2 respectively. In both cases data corresponding to $A_ik = 0.05$ (symbol ∘) and $A_ik = 0.10$ (symbol ∗) are shown. In addition, the solid line provides a comparison with the analytical solution by Sulisz (1993).

In both cases RB1 and RB2, it is clear that the second-order contribution becomes most significant in deep water. Sulisz (1993) demonstrated that the deep-water approximation for the second-order pressure upstream of the rectangular box ($x \leq -b$) is given by

$$p_{\mathrm{deep}}^{(2)} \approx -2\rho g A_i R_{11} k \quad \text{for} \quad x \leq -b, \tag{8}$$



(a) Configuration RB1



(b) Configuration RB2

Figure 6: Normalised second-harmonic of the vertical force due to incident regular waves with ▬ Sulisz (1993), ▬ ▬ approximation using dominant forcing term after equation (8), and ∘ MFBEM for $A_i k = 0.05$ and ∗ MFBEM for $A_i k = 0.10$.

where R_{11} is the amplitude of the first-order reflected wave. This second-order pressure term $p^{(2)}_{\text{deep}}$ arises due to the interaction of the first-order incident wave and the first-order reflected wave. For a constant incident wave amplitude A_i, the reflected wave amplitude R_{11} increases with kb, leading to an increase of the product kR_{11}. Furthermore, the second-order pressure in equation (8) is independent of the the depth z. In contrast, the first-order pressure term in deep water decays as e^{-kz}. Combining the two effects, the second-order pressure may become the dominant term in deep water.

The occurrence of depth-independent second-order pressures was first discussed by Longuet-Higgins and Ursell (1948), Longuet-Higgins (1950) and Cooper and Longuet-Higgins (1951). Indeed Longuet-Higgins and Ursell (1948) noted that this pressure generally arises in standing waves formed by two waves of equal frequency travelling in opposite directions. A more complete theoretical treatment, Longuet-Higgins (1950), established that the second-order pressure fluctuation in deep water is given by $-2\rho g A_1 A_2 k \cos(2\omega t)$, where A_1 and A_2 are the amplitudes of two progressive waves of frequency ω travelling in opposing directions. Within the experimental study by Cooper and Longuet-Higgins (1951), the second-order pressure field in the presence of a reflective structure was shown to be $-2\rho g A^2 \beta k \cos(2\omega t)$, where A is the amplitude of the incident progressive wave and β is the reflection coefficient. In the context of the present work, $A = A_i$ and $\beta = R_{11}/A_i$, so that the expression provided by Cooper and Longuet-Higgins (1951) is directly comparable to equation (8).

The approximation to the second-order pressure given in equation (8) is valid for $x \leq -b$. This pressure will, in turn, drive the fluid underneath the rectangular box. The dashed lines in Figures 6(a) and 6(b) illustrate the second-order heave force due to $p^{(2)}_{\text{deep}}$ only. To compute this force, all other interaction terms in the fluid region $x \leq -b$ were neglected, and the eigenfunction matching procedure defined in Sulisz (1993) was based on $p^{(2)}_{\text{deep}}$ alone. The approximation based upon this approach clearly accounts for the majority of the second-order heave force in deep water. In fact, for $kb > 0.3$ the approximation based upon this single forcing term provides a relatively close match to the full solution. This highlights the overall importance of the interaction between the first-order incident wave and the first-order reflected wave. On the basis of these calculations it is clear that the nonlinear forcing in the heave excitation problem is primarily driven by the interaction of the first-order incident and the first-order reflected wave, and is not associated with the second-order diffracted wave.

3.3. Wave steepness

All of the above cases relate to a constant wave steepness of $A_i k = 0.1$ for which second-order effects were shown to be significant. To explore this for a wider range of steepnesses ($A_i k$), the cases outlined in Table 1(b) were considered. The wave steepness was varied from

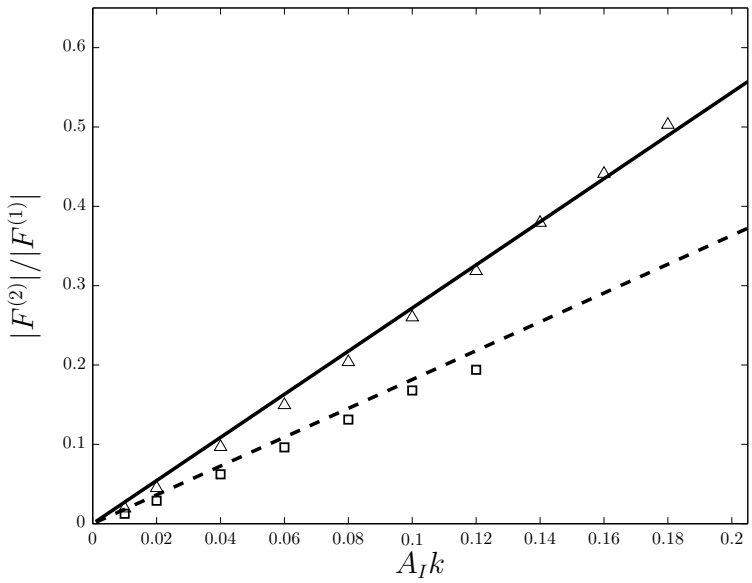


Figure 7: Ratio of second-harmonic vertical excitation force to its first-harmonic counterpart due to incident waves with $kh = 3$. Analytical solution by Sulisz (1993) with ▬ ▬ RB1, ▬▬ RB2 and MFBEM computations with □ RB1, △ RB2.

$0.01 \leq A_i k \leq 0.12$ for RB1 and $0.01 \leq A_i k \leq 0.18$ for RB2; the maximum wave steepness again being limited by the fixed draught d (Table 1(b)). The body dimension was chosen as $kb = 0.6$, corresponding to the scenario in which the floating body nonlinearity was found to be minimal (Figure 2), despite significant nonlinearity in the excitation forcing (Figures 4 and 6).

Figure 7 concerns the ratio of the second-harmonic vertical force $F^{(2)}$ to the corresponding first-harmonic force $F^{(1)}$ for cases RB1 (dashed line and symbol □) and RB2 (solid line and symbol △). The data clearly show that even for a moderate wave steepness the second-harmonic loads may account for as much as 50% of the first-harmonic loads. The nonlinearities are more pronounced for the deeper draught case, once again highlighting the importance of the depth-independent pressure term $p^{(2)}_{\text{deep}}$.

In considering the data small departures between the analytical solution and the numerical computations are observed (Figure 7), with an average departure of 4% and a maximum departure of up to 10%. It is believed that these departures are, in part, due to the occurrence of effects beyond second order. For example, at third order, the first-harmonic force $F^{(1)}$ will be affected, altering the ratio $F^{(2)}/F^{(1)}$. Whilst this effect is relatively small for the cases considered herein, $(A_i k)_{\max} = 0.18$, it will become larger with increased steepness. Unfortunately, an increased range of $A_i k$ is difficult to achieve for the present geometries. However, an extended range of $A_i k$ for alternative geometries is being considered as part of our ongoing work.

4. Part B: Investigation of the nonlinear radiation problem

4.1. Introduction and test parameters

In the context of the radiation problem, the wave field present within the NWT arises due to the prescribed motion of the body, $\xi(t)$. To quantify the nonlinearities associated with this problem, the relative body motion is expressed as a function of the body draught, d, leading to the non-dimensional ratio ξ_a/d, where ξ_a is the magnitude or amplitude of the body displacement. Three displacements were considered corresponding to (a) $\xi_a/d = 0.01$, (b) $\xi_a/d = 0.10$ and (c) $\xi_a/d = 0.25$.

Across these cases, the small displacements ($\xi_a/d = 0.01$) were included to serve as relatively linear reference cases. In these examples the MFBEM computations were compared to a linear reference calculation (again undertaken using WAMIT (2013)). This comparison confirmed that the MFBEM approach was capable of accurately computing the hydrodynamic coefficients (radiation damping and added mass); the maximum departure from the linear prediction being $< 3\%$. Having confirmed the linear predictions, the following discussion will focus on the description of the large amplitude cases, (b) and (c) above. Adopting the geometry described earlier, these cases are referred to as RB1b, RB2b, RB1c and RB2c. In all cases the frequency of the imposed motion was chosen such that the radiated waves lie within the range $0.2 \leq kb \leq 1.2$.

4.2. Radiated free waves

In the context of the radiation problem, all nonlinear forcing is due to the radiated wave field. As a consequence, it is instructive to first consider the nonlinear content of the radiated wave field. It is well known, particularly in the field of nonlinear wavemaking (Schäffer, 1996; Spinneken and Swan, 2009), that a sinusoidal body motion can lead to the generation of pronounced second-harmonic free waves. To investigate this effect, the second-harmonic of the radiated wave field was separated into its free and bound components. This was again achieved using the harmonic decomposition method proposed by Lin and Huang (2004) applied at $x \leq -(2h+b)$. Considering the progressive wave field alone, the harmonic decomposition yields a description of the radiated bound wave, $A_{rb}^{(2)}$, and the radiated free wave, $A_{rf}^{(2)}$, both arising at the second harmonic.

In a first step (not shown herein), the second-harmonic bound component $A_{rb}^{(2)}$ was directly compared to that calculated using Stokes' second-order theory; the maximum departure between the analytic solution and the MFBEM computations being $< 2\%$. This is exactly as expected and confirms the method of decomposition employed.

In a second step, the free wave content arising at the second harmonic was considered in detail. Figure 8 shows the ratio of the second-harmonic free wave to the second-harmonic

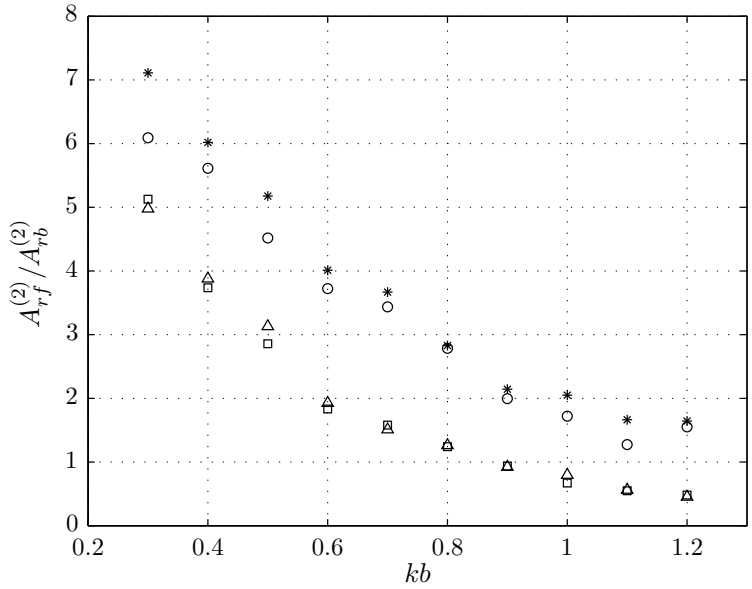


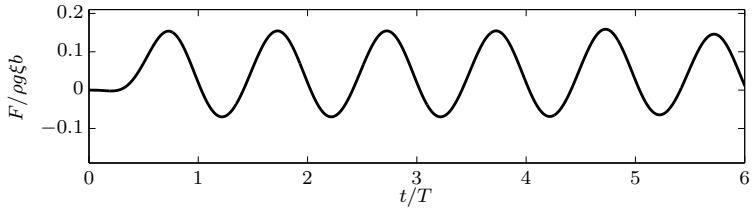
Figure 8: Ratio of second-harmonic free to second-harmonic bound component in the radiated field with ∘ RB1b ($\xi_a/d = 0.1$), ∗ RB1c ($\xi_a/d = 0.25$), △ RB2b ($\xi_a/d = 0.1$), and □ RB2c ($\xi_a/d = 0.25$).

bound wave component, $A^{(2)}_{rf}/A^{(2)}_{rb}$, for cases RB1b (symbol ∘), RB1c (symbol ∗), RB2b (symbol △) and RB2c (symbol □). As the normalised body dimension kb decreases, this ratio increases, suggesting a larger relative freely propagating second-harmonic component. This free wave component arises due to a mis-match in the second-order boundary condition on the surface of the body. Along the vertical sides of the rectangular box, the body boundary condition requires the normal fluid velocities to be zero. In contrast, on the underside of the box the fluid velocities are defined by $\partial\phi/\partial n = \mathbb{R}\{-i\omega\xi_a \exp(-i\omega t)\}$.

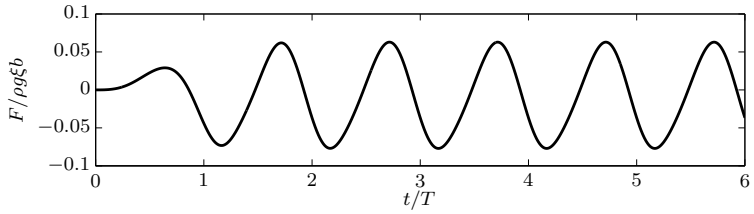
The enforced sinusoidal motion of the body only contains a single term of frequency ω. As a result, all higher harmonic terms must satisfy a no-flow condition on the body. At the same time, the nonlinear dynamic and kinematic free surface boundary conditions enforce a bound second-order Stokes' wave with an associated velocity field. The mismatch between this second-order bound velocity field and the no-flow condition on the body leads to the generation of an additional free wave; the physics being very similar to the well-known (nonlinear) wavemaker problem. With increasing wave frequency (corresponding to increasing kb), the second-order bound wave content decays rapidly over depth z, and is likely to be insignificant on the underside of the box at $z = -d$. As a result, the forcing boundary condition at this location is less significant as kb increases. This explains the decrease of $A^{(2)}_{rf}/A^{(2)}_{rb}$ with increasing kb in Figure 8.

4.3. Nonlinear radiation forcing due to large body excursions

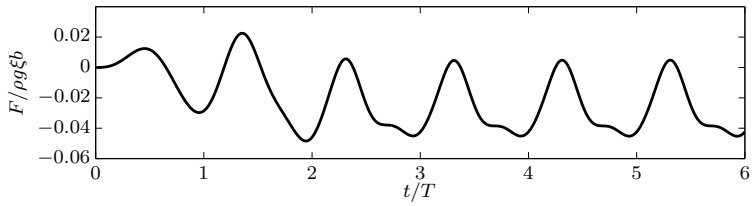
Figure 9 concerns the nonlinearities associated with the radiation force providing sample time histories relating to cases (a) $kb = 0.2$, (b) $kb = 0.6$ and (c) $kb = 1.2$; the displacement



(a) $kb = 0.2$



(b) $kb = 0.6$



(c) $kb = 1.2$

Figure 9: Time history of the radiation force on a heaving box of configuration RB2 subjected to body excursions of $\xi/d = 0.25$.

being defined by $\xi_a/d = 0.25$ in all cases. It is clear from this figure that the nonlinearity of the radiation force becomes more pronounced as kb increases. This is in marked contrast to the increase of the second-harmonic free wave with decreasing kb (Figure 8). To demonstrate this further, the second harmonic of the radiation force is illustrated in Figure 10; the adopted normalisation, $F^{(2)}/\rho g\xi_a^2$, being similar to that adopted in the existing literature (§1.1). The magnitude of the relative first-harmonic component of the radiation force (not shown herein) decreases with increasing kb, whilst the magnitude of the second-harmonic force component increases (Figure 10). As a result, the relative importance of the second-harmonic force component will increase significantly as kb increases. This increase in the relative importance of the second-harmonic radiation force is consistent with earlier work of Zhou et al. (2013) concerning truncated vertical columns, and is also evident in the time histories displayed in Figure 9.

Unfortunately, the normalisation by $\rho g\xi_a^2$ does not take into account that a particular body motion ξ_a/d leads to very different radiated wave amplitudes as kb varies. Generally speaking, the body motion required to radiate a wave of particular amplitude A_{rad} increases significantly as kb decreases. As a result, it may be argued that the actually radiated wave amplitude A_{rad} provides a more suitable basis for the second-harmonic force normalisation. To illustrate this, the data presented in Figure 10 are re-plotted in Figure 11, using a revised

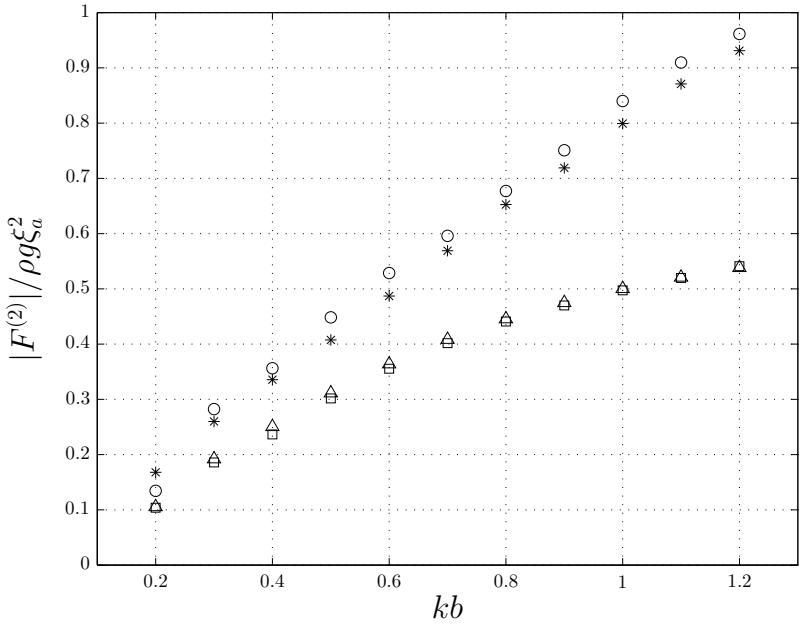


Figure 10: Normalised second-harmonic vertical radiation force $F^{(2)}/\rho g\xi_a^2$ with $\circ$ RB1b ($\xi_a/d = 0.1$), $*$ RB1c ($\xi_a/d = 0.25$), $\triangle$ RB2b ($\xi_a/d = 0.1$), and $\square$ RB2c ($\xi_a/d = 0.25$).

normalisation factor $\rho g A_{\rm rad}^2$.

Comparisons between Figures 10 and 11 reveal some key features of the nonlinear radiation problem. Within Figure 10, the second-harmonic force was seen to increase monotonically with increasing kb. In marked contrast, Figure 11 shows a significantly more complex variation of this force component. For the shallower draught, configuration RB1 (symbol $\circ$ and $*$), the second-harmonic force shows a distinct minimum in the range $0.6 \leq kb \leq 0.8$. As kb decreases below 0.6, the radiation force $F^{(2)}/\rho g A_{\rm rad}^2$ increases. This is consistent with the increase of the second-harmonic free wave within this regime (Figure 8). In the range $0.2 \leq kb \leq 0.4$, the second-harmonic forcing for RB1 exceeds that of RB2. This is again is consistent with the findings of Figure 8.

As kb increases beyond the location of the force minimum ($kb > 0.8$), the second-harmonic force again increases. In this regime, the second-harmonic free wave is relatively small (Figure 8), and does not entirely account for the second-harmonic forcing. However, it is well known that the radiation problem is also associated with a local standing wave field arising at each order. To investigate the magnitude of this local standing wave field, the second-harmonic of the wave runup on the body face, at $x = -b$, was considered in detail. The results of this analysis are shown in Figure 12, where the second-harmonic runup, $\zeta^{(2)}$, was normalised by the radiated wave amplitude $A_{\rm rad}$. This normalisation is dimensionless in terms of physical units, but is inconsistent in respect of the order of the terms involved. As a result, the data points for $\xi/d = 0.1$ and $\xi/d = 0.25$ lie approximately a factor 2.5 apart.

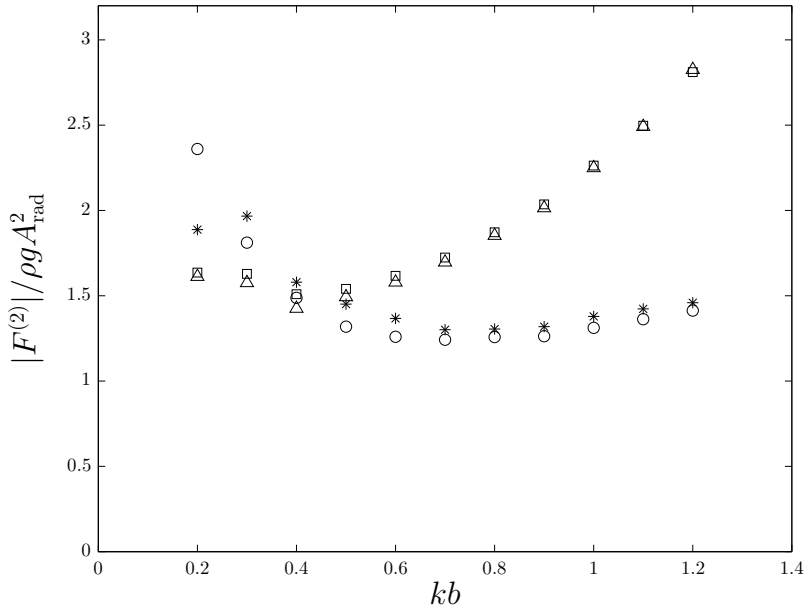


Figure 11: Normalised second-harmonic heave radiation force $F^{(2)}/\rho g A_{\rm rad}^2$ with $\circ$ RB1b ($\xi_a/d = 0.1$), $*$ RB1c ($\xi_a/d = 0.25$), $\triangle$ RB2b ($\xi_a/d = 0.1$) and $\square$ RB2c ($\xi_a/d = 0.25$).

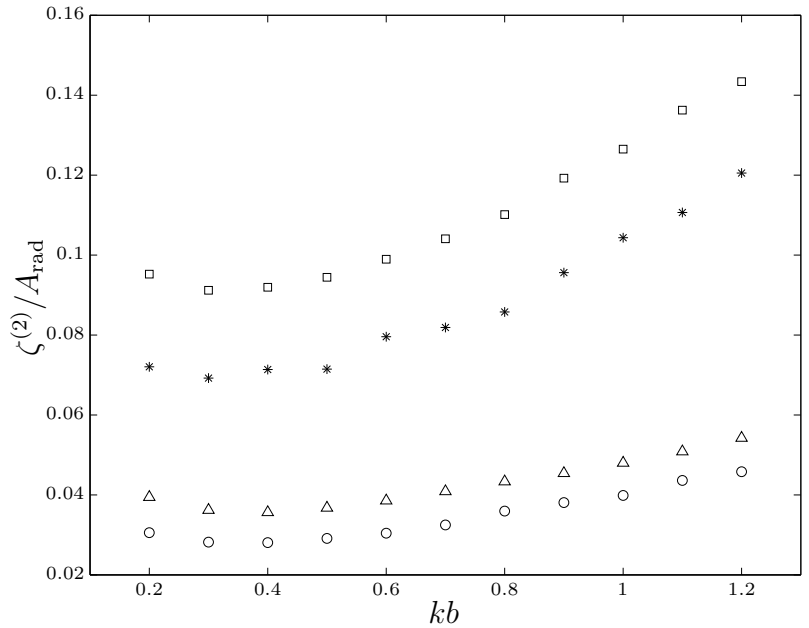


Figure 12: Normalised second-harmonic $\zeta^{(2)}/A_{\rm rad}$ with $\circ$ RB1b ($\xi_a/d = 0.1$), $*$ RB1c ($\xi_a/d = 0.25$), $\triangle$ RB2b ($\xi_a/d = 0.1$) and $\square$ RB2c ($\xi_a/d = 0.25$).

Nevertheless, the normalisation chosen demonstrates that the magnitude of the second-harmonic runup is significant when compared to the radiated wave amplitude, with $\zeta^{(2)}/A_{\mathrm{rad}}$ reaching up to 14%. Perhaps more importantly, this magnitude increases with increasing kb (Figure 12). In contrast, the second-harmonic free wave amplitude decreases with increasing kb. This suggests that a significant amount of the second-harmonic runup is associated with a local standing wave field, which contributes to the overall forcing. In considering Figure 12, it can also be observed that the second-harmonic runup for RB2 is more pronounced than that for RB1, whereas the opposite is true for the magnitude of the freely propagating second-harmonic wave (Figure 8). As a direct consequence, the second-harmonic forcing for RB2 is also more pronounced as kb increases (Figure 11) where the loading is predominately due to the local standing wave field. Taken as a whole, the behaviour of the second-harmonic radiation force, associated with both propagating and standing waves, may provide a sound basis for the floating body behaviour observed on Figure 2. This is discussed in the following section.

5. Part C: Investigation of the coupled floating problem

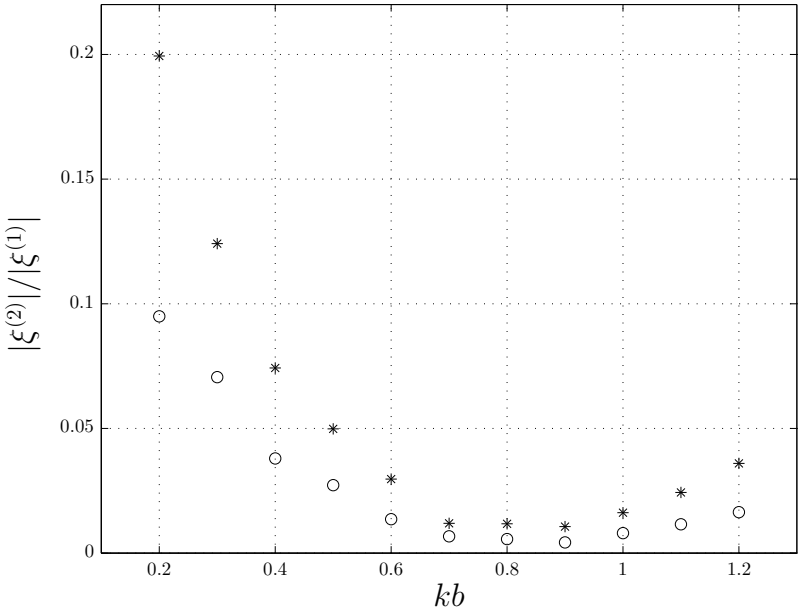
The discussion given above has identified a number of sources of the nonlinear loads, arising in both the excitation and the radiation problems. In considering the excitation forces, the interaction between the first-order incident wave and the first-order reflected wave was found to be most important, particularly as kb increases. Within the radiation problem, the nonlinear forcing was found to be driven by the radiated second-harmonic free wave, associated with both the progressive and standing wave modes.

To investigate the importance of these loads on the overall heave displacement, a harmonic decomposition of the heave motions was undertaken for the full range of cases ($0.2 \leq kb \leq 1.2$, $A_ik = 0.05$ and $A_ik = 0.1$). The results of this analysis are shown in Figures 13(a) and 13(b) for RB1 and RB2 respectively. These show the magnitude of the second-harmonic box displacement $\xi^{(2)}$ normalised by the first-harmonic displacement $\xi^{(1)}$. As the incident wave steepness increases, the relative importance of the second-harmonic component of the body motion increases, a similar pattern being observed for both geometries. For example, whilst the second-harmonic motions only account for up to 12% for $A_ik = 0.05$, this increases to up to 24% for $A_ik = 0.10$ (Figure 13(b)).

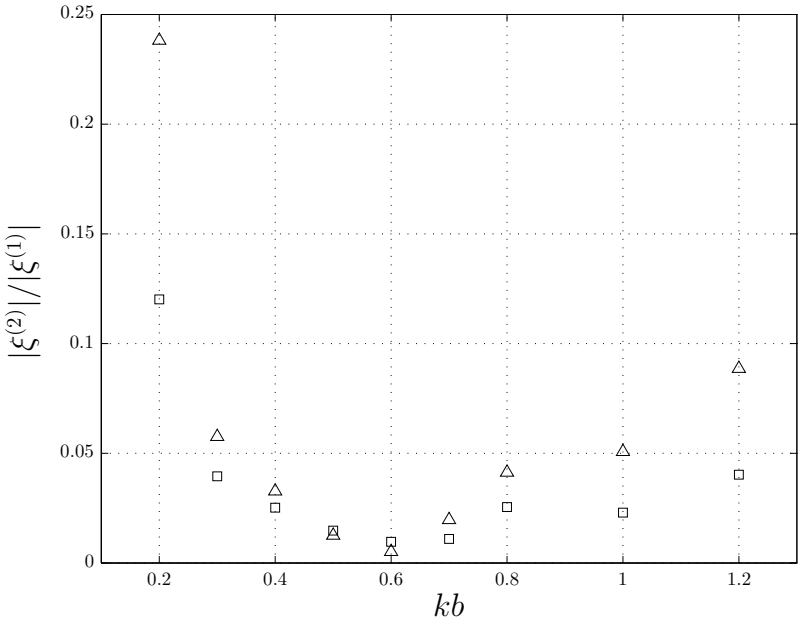
In comparing Figures 13(a) and 13(b), several similarities are observed, but some differences are also present. First, the second-harmonic content in both configurations RB1 and RB2 exhibits a *U-shaped* pattern. The most pronounced nonlinearities arise for the longest waves with $kb = 0.2$. However, in the short wave limit, $kb = 1.2$, the nonlinearities also exhibit an increasing trend. For intermediate values of kb a minimum is clearly established. For box RB1 in Figure 13(a), this minimum occurs at $kb \approx 0.8$, whilst in box RB2 (Figure 13(b)) it is shifted to $kb \approx 0.6$.

Whilst the distinct *U-shaped* pattern may have been expected given the discussion outlined above, it is perhaps surprising that the nonlinear excitation is more pronounced for low kb. Considering the nonlinear heave motion in Figure 13, it might be inferred that the nonlinear forcing at large kb ($kb \approx 1.2$) is less pronounced than that at $kb \approx 0.2$. However, this is misleading, not least because the heave motions are dependent upon both the applied loads and the frequency-dependence of the system response; the latter modelled in a linear sense using a Response Amplitude Operator or RAO (Figure 1). The dynamics of the problem are clearly dependent upon the frequency of force excitation. For all cases considered herein, the wave frequency associated with the second-harmonic frequency, $\omega^{(2)} = 2\omega^{(1)}$, corresponds to a relatively deep water wave. Based on this assumption, it is readily shown that $k^{(2)}h \approx 4k^{(1)}h \tanh k^{(1)}h$, where $k^{(2)}$ is the wave number corresponding to free waves at $\omega^{(2)}$, and $k^{(1)}$ is the fundamental wave number.

Combining the nonlinear forcing and the dynamic response gives rise to three distinct



(a) Configuration RB1 subjected to regular waves with $A_i k = \circ$ 0.05 and $*$ 0.10.



(b) Configuration RB2 subjected to regular waves with $A_i k = \square$ 0.05 and $\triangle$ 0.10.

Figure 13: Second-harmonic content in the box heave motion, $\xi^{(2)}$, normalised by the first-harmonic motion content $\xi^{(1)}$.

regimes in terms of the heave motion:

(i) In the long wave regime, with $kb \leq 0.4$, the nonlinear forcing is primarily driven by the radiation problem (Figure 11); the nonlinear forcing due to the excitation problem having been shown to be relatively small (Figure 6). Most importantly, the frequency of the second-harmonic forcing is such that it lies in close proximity to the resonance frequency (Figure 1). For example, $k^{(1)}b = 0.20$ corresponds to $k^{(2)}b = 0.6$, which is close to the resonant frequency of RB1 (Figure 1). Likewise, the corresponding resonant excitation of RB2 occurs at $k^{(1)}b = 0.23$, giving $k^{(2)}b = 0.8$. The combination of the nonlinear radiation forcing and the proximity of the resonance condition are the primary drivers for the large second-harmonic motions in the long wave regime (Figure 13).

(ii) In the intermediate wave regime, with $0.4 < kb < 1.0$, the nonlinear forcing due to the radiation problem becomes relatively small (Figure 11). However, the component of the nonlinear forcing due to the excitation problem is more pronounced. Nevertheless, it remains smaller than that which occurs in the short wave regime (Figure 6). For $k^{(1)}b = 0.6$ the second-harmonic forcing occurs at $k^{(2)}b = 2.4$, for which the RAO is relatively small (<0.1 for both RB1 and RB2). The combination of limited nonlinear forcing and a lack of dynamic excitation leads to the small second-harmonic motions observed on Figure 13.

(iii) In the short wave regime, with $kb \geq 1.0$, the standing wave fields due to both the radiation problem and the excitation problem are of critical importance. This leads to substantial nonlinear forcing in this regime. Despite the very large second-harmonic forces, the second-harmonic motions in the short wave regime are less pronounced when compared with the long wave regime. This is due to small RAOs; the latter being dominated by the body inertia at high frequencies.

Taken as a whole, the nonlinear forcing is most pronounced in the short wave regime, outlined in (iii) above. However, the combination of moderate nonlinear forcing and a pronounced dynamic response ensures that the long wave regime is more susceptible to large second-harmonic motions. Furthermore, this interpretation also notes that if the RAO is narrow banded, this leads to a very narrow banded response of the second-harmonic motion. Clear evidence of this is provided by the comparison between Figures 13(a) and 13(b); the latter being consistent with the shape of the RAOs given in Figure 1.

6. Concluding remarks

The paper has highlighted the importance of nonlinearity in the description of a heaving rectangular box. Most importantly, these nonlinearities were shown to produce a significant second-harmonic heave motion, even in moderately steep incident waves. By separating the problem into its component parts, the second-harmonic content was shown to follow a distinct *U-shaped* pattern. This has pronounced nonlinear content in both the long wave and the short wave or diffraction regime. In the diffraction regime, the primary sources of the nonlinear loads were identified as two standing wave fields; one due to the interaction between the first-order incident and the first-order reflected wave, and one due to the body motion.

The influence of the second-harmonic scattered wave as part of the fixed-body problem is very limited. In contrast, the second-harmonic radiated wave due to the body motion makes some very important contributions to the overall nonlinearity of the problem. Taken as a whole, the most pronounced second-harmonic motions were found where a particular load term occurs in close vicinity to the resonance of the box. If the resonance is narrow banded, then this also leads to a narrow banded response in terms of the second-harmonic heave motion. This latter observation has important implications for offshore model testing or numerical modelling, which could potentially fail to detect such a narrow-banded nonlinear response.

Whilst the present work has focused on a heaving rectangular box, the findings are more generally applicable. This is particularly true of alternative two-dimensional geometries such as a wedge or a submerged cylinder. Whilst the exact numerical values for forces (and motions) depend upon the specific geometry, a substantial amount of the underpinning physical understanding can be translated. In the excitation problem, the dominant force component was associated with the interaction between the first-order incident and the first-order reflected wave. This interaction is not specific to the rectangular box. Indeed, as already noted in the work by Cooper and Longuet-Higgins (1951), this interaction term arises for any reflective structure. As a result, the importance of this term is readily established by considering the reflection properties of the geometry under investigation; the latter easily obtained through a first-order analysis.

In a floating body context, the distinct *U-shaped* pattern observed also has wide applications. The exact nature of this pattern depends on at least three properties of the structure including: (i) the wave reflection behaviour, (ii) the radiation behaviour and (iiii) the resonance behaviour. The first has already been noted above, and is responsible for the short-wave or diffraction part of the *U-shaped* pattern ($kb \geq 1.0$). The radiation behaviours of common two-dimensional geometries such as a wedge or a cylinder are well understood,

as these have been considered in the context of wavemaking; relevant accounts being given in Frank (1967) and Koo and Kim (2006). If this radiation behaviour leads to significant second-harmonic forcing at the resonance frequency, the long-wave ($kb \leq 0.4$) related rise in the *U-shaped* pattern is also expected to be independent of the geometry considered.

The present study has focused on effects arising at second harmonic under regular wave excitation. Ongoing work includes numerical computations in the context of transient wave groups, an analysis of effects beyond the second-harmonic, an extension of the work to three-dimensions, and an experimental validation of the present findings.

Acknowledgement

The first author would like to acknowledge the financial support provided through the BEIT Fellowship for Scientific Research, which has enabled this research. The work presented herein has also received financial support through UK EPSRC Grant EP/J010197/1.

Bai, W. and Eatock Taylor, R. (2006), 'Higher-order boundary element simulation of fully nonlinear wave radiation by oscillating vertical cylinders', *Applied Ocean Research* **28**(4), 247–265.

Christou, M., Hague, C. and Swan, C. (2009), 'The reflection of nonlinear irregular surface water waves', *Eng. Anal. Bound. Elem.* **33**, 644–653.

Christou, M., Swan, C. and Gudmestad, O. (2008), 'The interaction of surface water waves with submerged breakwaters', *Coastal Engineering* **55**, 945–958.

Cooper, R. and Longuet-Higgins, M. S. (1951), 'An experimental study on the pressure variations in standing water waves', *Proceedings of the Royal Society of London. A.* **206**, 424 – 435.

Eatock Taylor, R. and Hung, S. (1987), 'Second-order diffraction forces on a vertical cylinder in regular waves', *Applied Ocean Research* **9**, 19–30.

Fenton, J. (1985), 'Fifth Order Stokes Theory for Steady Waves', *Journal of Waterway, Port, Coastal and Ocean Engineering* **111**(2), 216–234.

Ferrant, P., Touze, D. L. and Pelletier, K. (2003), 'Non-linear time-domain models for irregular wave diffraction about offshore structures', *International Journal for Numerical Methods in Fluids* **43**, 1257–1277.

Frank, W. (1967), Oscillation of cylinders in or below the free surface of deep oscillation of cylinders in or below the free surface of deep fluids, Technical Report 2375, Naval Ship Research and Development Center.

Grilli, S. and Horrillo, J. (1997), 'Numerical Generation and Absorption of Fully Nonlinear Periodic Waves', *Journal of Engineering Mechanics* **123**(10), 1060–1069.

Hague, C. and Swan, C. (2009), 'A multiple flux boundary element method applied to the description of surface water waves', *Journal of Computational Physics* **228**(14), 5111–5128.

Kashiwagi, M. (2000), Non-linear simulations of wave-induced motions of a floating body by means of the mixed Eulerian-Lagrangian method, *in* 'Proceedings of the Institution of Mechanical Engineers. Part C: Jounral of Mechanical Engineering Science'.

Kim, M. and Yue, D. (1989), 'The complete second-order diffraction solution for an axisymmetric body. Part 1: Monochromatic incident waves', *Journal of Fluid Mechanics* **200**, 235–264.

Kim, M. and Yue, D. (1990), 'The complete second-order diffraction solution for an axisymmetric body: Part 2. Bichromatic incident waves and body motions', *Journal of Fluid Mechanics* **211**, 557–593.

Koo, W. and Kim, M. (2006), 'Numerical simulation of nonlinear wave and force generated by a wedge-shape wave maker', *Ocean Engineering* **33**, 983–1006.

Lighthill, J. (1979), Waves and hydrodynamic loading, *in* 'Proceedings of the Second International Conference on the Behaviour of Offshore Structures'.

Lin, C.-Y. and Huang, C.-J. (2004), 'Decomposition of incident and reflected higher harmonic waves using four wave gauges', *Coastal Engineering* **51**(5–6), 395 – 406.

Longuet-Higgins, M. S. (1950), 'A theory of the origin of microseisms', *Philosophical Transactions of the Royal Society A* **243**, 1–35.

Longuet-Higgins, M. S. and Cokelet, E. D. (1976), 'The Deformation of Steep Surface Waves on Water. I. A Numerical Method of Computation', *Proceedings of the Royal Society of London. A. Mathematical and Physical Sciences* **350**(1660), 1–26.

Longuet-Higgins, M. S. and Ursell, F. (1948), 'Sea waves and microseisms', *Nature* **162**, 700.

Ma, Q. W., Wu, G. X. and Eatock Taylor, R. (2001), 'Finite element simulation of fully nonlinear interaction between vertical cylinders and steep waves. part 1: methodology and numerical procedure', *International Journal for Numerical Methods in Fluids* **36**, 265–285.

Maiti, S. and Sen, D. (2001), 'Nonlinear heave radiation forces on two-dimensional single and twin hulls', *Ocean Engineering* (28), 1031–1052.

Molin, B. (1979), 'Second-order diffraction loads upon three-dimensional bodies', *Applied Ocean Research* **1**(4), 197–202.

Molin, B. and Marion, A. (1985), Etude au deuxieme ordre du comportement des corps flottants en houle reguliere, Technical Report 8334008004707501, Insitute Francais du Petrole.

Schäffer, H. (1996), 'Second-order wavemaker theory for irregular waves', *Ocean Engineering* **23**, 47–88.

Spinneken, J., Christou, M. and Swan, C. (2014), 'Force-controlled absorption in a fully-nonlinear numerical wave tank', *Journal of Computational Physics* **272**, 127.

Spinneken, J. and Swan, C. (2009), 'Second-order wave maker theory using force-feedback control. Part I: A new theory for regular wave generation', *Ocean Engineering* **36**(8), 539 – 548.

Sulisz, W. (1993), 'Diffraction of second order surface waves by semisubmerged horizontal rectangular cylinder', *Journal of Waterway, Port, Coastal, and Ocean Engineering* **119**(2), 160–171.

Tanizawa, K. (1995), 'A nonlinear simulation method of 3-d body motions in waves', *Journal of the Society of Naval Architects of Japan* **178**, 179–191.

WAMIT (2013), *WAMIT User Manual: Version 7.0*, WAMIT Inc, `www.wamit.com`.

Wu, G. and Eatock Taylor, R. (1996), Transient motion of a floating body in steep water waves, *in* 'Proceedings of the 11th International Workshop on Water Waves and Floating Bodies', Hamburg, Germany, pp. 219–223.

Xue, M., Xu, H., Liu, Y. and Yue, D. K. P. (2001), 'Computations of fully nonlinear three-dimensional wave body interactions. part 1. dynamics of steep three-dimensional waves', *Journal of Fluid Mechanics* **438**, 11–39.

Zhou, B., Ning, D., Teng, B. and Bai, W. (2013), 'Numerical investigation of wave radiation by a vertical cylinder using a fully nonlinear HOBEM', *Ocean Engineering* (70), 1–13.